Research Square

Preprints are preliminary reports that have not undergone peer review.
They should not be considered conclusive, used to inform clinical practice,
or referenced by the media as validated information.

MetaLFM: Metalens-array-enabled High-Density Optical Sampling for High-Resolution Volumetric Bioimaging by Light Field Microscopy

Euiheon Chung

ogong50@gist.ac.kr

Gwangju Institute of Science and Technology

Tien Nhat Nguyen

Gwangju Institute of Science and Technology

Doyoon Lee

Gwangju Institute of Science and Technology

Huu Lam Phan

Gwangju Institute of Science and Technology

Akm Ashiquzzaman

Gwangju Institute of Science and Technology

Yesl Jun

Korea Research Institute of Chemical Technology

Minkyung Kim

Gwangju Institute of Science and Technology https://orcid.org/0000-0001-5229-4520

Article

Keywords: metalens, light field imaging, volumetric imaging, calcium imaging, 3D microscopy

Posted Date: September 28th, 2026

DOI: https://doi.org/10.21203/rs.3.rs-10896258/v1

License: This work is licensed under a Creative Commons Attribution 4.0 International License.
Read Full License

Additional Declarations: There is no conflict of interest

MetaLFM: Metalens-array-enabled High-Density Optical Sampling for High-Resolution Volumetric Bioimaging by Light Field Microscopy

Tien Nhat Nguyen[1 †], Doyoon Lee[2,†], Huu Lam Phan[3,4], Akm Ashiquzzaman[1], Yesl Jun[5,6], Minkyung Kim[2,], Euiheon Chung[1,7,*]*

[1]Department of Biomedical Science and Engineering, Gwangju Institute of Science and Technology, 61005 Gwangju, Republic of Korea.

[2]Department of Mechanical and Robotics Engineering, Gwangju Institute of Science and Technology, 61005 Gwangju, Republic of Korea

[3]GIST InnoCORE AI-Nano Convergence Institute for Early Detection of Neurodegenerative Diseases, Gwangju Institute of Science and Technology, 61005 Gwangju, Republic of Korea

[4] Mechatronics and Robotics Research Group, Faculty of Engineering and Technology, Nguyen Tat Thanh University, Ho Chi Minh City 754000, Vietnam

[5]Therapeutics & Biotechnology Division, Korea Research Institute of Chemical Technology, Daejeon 34114, Republic of Korea

[6]Department of Medicinal Chemistry and Pharmacology, University of Science and Technology, Daejeon 34113, Republic of Korea

[7]AI Graduate School, Gwangju Institute of Science and Technology, 61005 Gwangju, Republic of Korea

† These authors contributed equally to this work

*Corresponding author: m.kim@gist.ac.kr, ogong50@gist.ac.kr

Abstract:

Light field microscopy enables snapshot volumetric imaging by simultaneously capturing spatial and angular information. However, its imaging performance is fundamentally governed by the sampling geometry of the microlens array. Increasing the sampling density through reduced lens pitch is desirable for improving spatial resolution yet implementing small-pitch refractive microlens arrays while maintaining the focal length and f-number required for LFM becomes increasingly challenging because of geometric fabrication constraints. Here, we present MetaLFM,

a metalens-array-enabled high-density optical sampling architecture for high-resolution volumetric bioimaging. A large-area TiO_2 metalens array with a 75-μm pitch and a designed focal length of 1430 μm was engineered to provide reduced-pitch sampling while maintaining the f-number matching condition required for light field acquisition. Experimental characterization demonstrated consistent focusing performance across the fabricated array and confirmed a stable operating condition for spatial–angular light-field sampling. Compared with conventional LFM using a 100-μm-pitch refractive microlens array, MetaLFM reduced the reconstructed lateral and axial full width at half maximum by up to 44% and 39%, respectively, across the evaluated imaging depth, while reducing grid-like reconstruction artifacts near the native image plane. Volumetric imaging of mouse spinal cord tissue and human intestinal organoids showed improved structural delineation and reconstruction fidelity, while 25 Hz calcium imaging of primary cortical neurons demonstrated applicability to dynamic bioimaging. These results expand the resolution–depth capabilities of light field microscopy for high-resolution volumetric bioimaging.

Keywords: metalens, light field imaging, volumetric imaging, calcium imaging, 3D microscopy

1. Introduction

Imaging biological systems requires resolving three-dimensional (3D) structures with high spatial resolution and temporal throughput, as key processes such as neuronal signaling, blood circulation, and tissue morphogenesis occur across extended volumes and evolve on millisecond timescales. Conventional volumetric fluorescence imaging techniques, including confocal microscopy [1], multiphoton microscopy [2], and light sheet microscopy [3], achieve 3D imaging through optical sectioning or engineered point spread functions (PSF) [4]. However, these approaches rely on sequential acquisition of multiple focal planes or additional optical encoding, which increases system complexity and limits volumetric imaging speed [5].

Light field microscopy (LFM) provides an alternative approach by capturing both spatial and angular information of light within a single snapshot. By incorporating a microlens array (MLA) in front of the image sensor, LFM records a 4D light field that can be computationally reconstructed into a 3D volume [6–8]. This snapshot-based acquisition enables high-speed volumetric imaging and offers a compact framework for computational microscopy. In this framework, imaging performance is governed by the sampling geometry imposed by the MLA. This architecture inherently introduces a trade-off between spatial resolution and depth-of-field (DOF), since both quantities are jointly determined by the distribution of spatial and angular samples. Specifically, the MLA pitch and the objective lens parameters define the achievable resolution and depth range (Supplementary Note 1). Increasing the objective magnification improves spatial resolution at the expense of imaging depth [6,9]. However, this approach does not resolve the intrinsic limitation of LFM, where spatial and angular information are multiplexed onto a finite sensor.

Consequently, higher magnification reduces the DOF and leads to depth-dependent degradation in resolution, limiting the fidelity of volumetric reconstruction [6,9].

Alternatively, reducing the MLA pitch improves spatial resolution in light field microscopy (Fig. 1b). In LFM, strict f-number ($f^{\#}$) matching enforces an inherent coupling between lens pitch and focal length (Supplementary Note 1), requiring proportionally shorter focal lengths as the pitch decreases. Such scaling is incompatible with refractive microlenses, where extreme curvature and large sag height impose prohibitive fabrication constraints [10,11]. Consequently, further reduction of refractive microlens pitch under strict $f^{\#}$ matching becomes increasingly challenging in practice. As a result, achievable pitch scaling remains limited in typical implementations [12–16]. Existing approaches have therefore focused primarily on computational reconstruction or illumination engineering rather than modifying the underlying optical sampling architecture, leaving the pitch-scaling limitation of refractive MLAs unresolved and constraining further improvements in spatial resolution and volumetric reconstruction fidelity. This motivates an alternative optical architecture capable of realizing reduced-pitch sampling while maintaining the required focal length and $f^{\#}$.

Recent advances in metasurface photonics represent a paradigm shift that overcomes the intrinsic limitations of conventional microlens arrays [17]. By replacing curvature-based focusing with subwavelength phase engineering, metalenses provide flexible control over focal length and numerical aperture within a planar optical architecture [17,18]. This design flexibility provides a route to spatial–angular sampling regimes that are difficult to realize with conventional refractive MLAs. Although metalens arrays have been demonstrated in light field photography at the mesoscale [19–25], their extension to microscopic imaging remains largely unexplored. In particular, no prior work has realized metalens-array-based light field microscopy with reduced lens pitch for volumetric

bioimaging. This capability is essential, as pitch scaling directly increases angular sampling density, which in turn improves spatial resolution, suppresses reconstruction artifacts, and enhances volumetric fidelity.

In this work, we demonstrate a metalens-array-based light field microscopy architecture (Fig. 1a) that realizes improved spatial resolution while maintaining comparable depth performance through a reduced-pitch metalens array (MeLA). By leveraging nanoscale wavefront engineering, the proposed system achieves efficient transmission and full phase control, and is experimentally implemented as a large-area metalens array (60 × 60 lenses, ~4.5 mm × 4.5 mm) with a lens diameter of 71.5 μm using nanoscale lithography (Fig. 1c, d). Volumetric imaging of human intestinal organoids reveals enhanced structural resolution (~20–25% improvement) and suppressed grid-like reconstruction artifacts inherent to MLA-based systems (Fig. 1e). These results establish MeLA as a viable route to surpass the sampling limitations of conventional light field microscopy and provide a new optical sampling strategy for volumetric bioimaging.

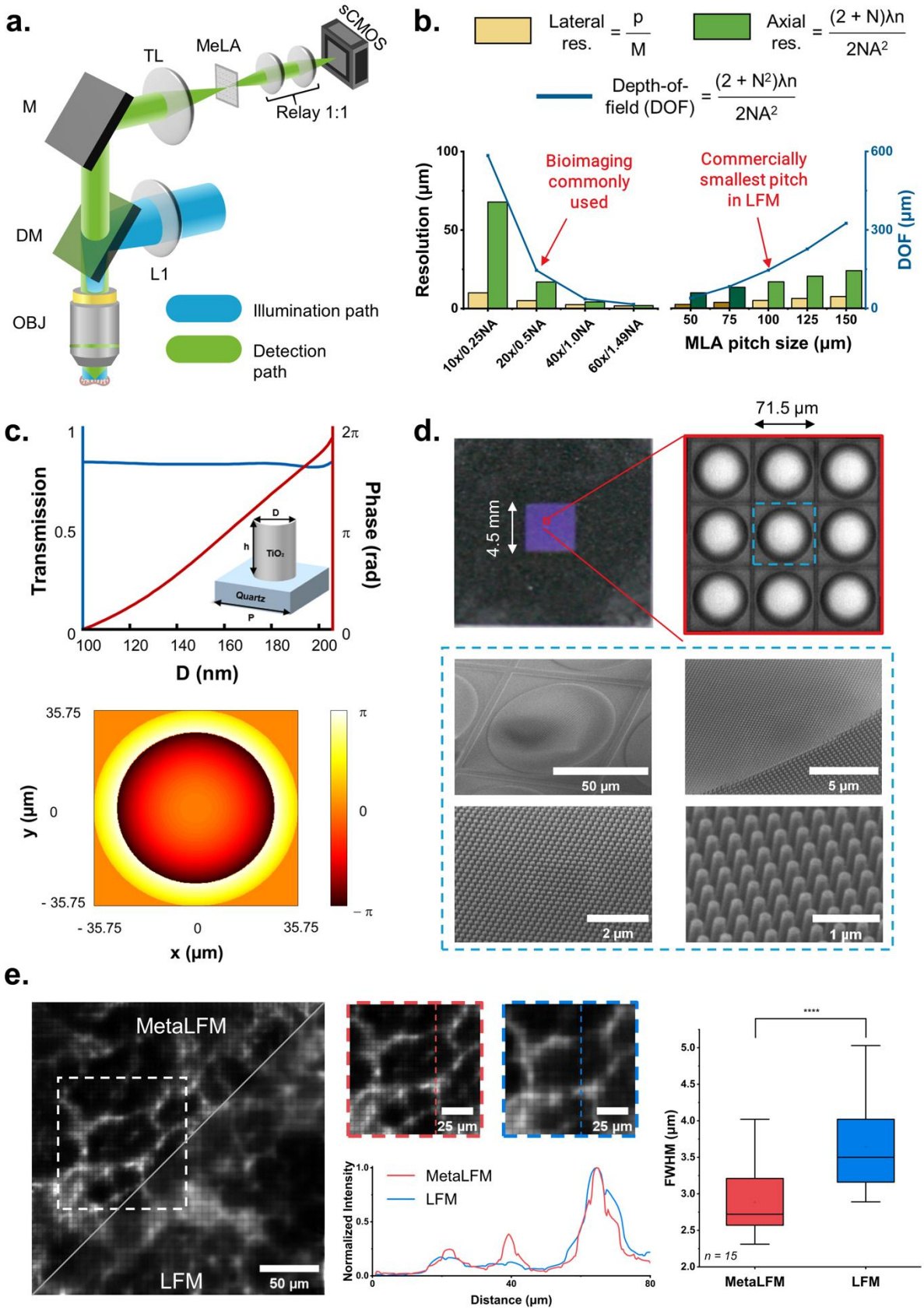

a.
sCMOS
TL
MeLA
M
Relay 1:1
DM
L1
OBJ
Illumination path
Detection path
b.
Lateral res. = p / M
Axial res. = (2 + N)λn / 2NA²
Depth-of-field (DOF) = (2 + N²)λn / 2NA²
Resolution (μm)
DOF (μm)
Bioimaging commonly used
Commercially smallest pitch in LFM
10x/0.25NA
20x/0.5NA
40x/1.0NA
60x/1.49NA
MLA pitch size (μm)
c.
Transmission
Phase (rad)
D (nm)
TiO₂
Quartz
y (μm)
x (μm)
d.
71.5 μm
4.5 mm
50 μm
5 μm
2 μm
1 μm
e.
MetaLFM
LFM
50 μm
25 μm
25 μm
Normalized Intensity
Distance (μm)
FWHM (μm)
n = 15
****

*Figure 1. MetaLFM concept: (a) Schematic of the MetaLFM optical system, where the conventional microlens array (MLA) in light field microscopy is replaced by a metalens array (MeLA). (b) Illustration of the trade-off between spatial-resolution and DOF in conventional LFM and the design strategy for improving this trade-off by reducing lens pitch. M is the objective magnification, NA is the objective numerical aperture. p is the MLA pitch size, N is the resolvable spots, λ is the emission wavelength, n is the refractive index. (c) Simulated transmission and phase response of the meta-atom as a function of nanopillar diameter, demonstrating high transmission efficiency and full 0–2π phase coverage for constructing the metalens phase profile; the calculated phase distribution of the designed metalens is shown below. (d) Structural characterization of the fabricated MeLA, including optical microscopy images of the lens array and SEM images of individual metalenses (lens diameter, 71.5 μm). (e) Average intensity projection (AIP) of a reconstructed intestinal organoid comparing MetaLFM and conventional LFM. MetaLFM reveals sharper structural features and reduced grid-like artifacts. Enlarged regions of interest (ROIs) with corresponding intensity profiles extracted along dashed lines demonstrate enhanced structural resolution. "****" indicates $p < 0.0001$.*

2. Results

2.1. Characterization of MeLA

To validate the metalens-array-enabled sampling architecture, the optical performance of the fabricated metalens array (MeLA) was characterized through numerical simulations and experimental measurements at both the single-lens and array levels. The focal characteristics are summarized in Fig. 2a, with the corresponding experimental setup shown in Fig. S3. The simulated and measured axial and lateral intensity distributions show close agreement, confirming that the fabricated MeLA reproduces the designed optical response. The upper panels present the calculated distributions obtained using a propagation model, whereas the lower panels show the corresponding experimental measurements. The MeLA was designed with a focal length of 1430 μm to satisfy the $f^{\#}$ matching condition of the LFM system. Both simulation and experiment show that the on-axis intensity reaches its maximum at a shorter axial distance of approximately 1240 μm. This offset is consistent with deviations from the ideal continuous phase response introduced

by the discrete unit-cell implementation and the local periodic approximation, with the low numerical aperture of the lens potentially contributing further through edge-diffraction effects [26]. Importantly, the peak-intensity position remains within the broad axial focusing envelope of the MeLA, which has an axial full width at half maximum (FWHM) of approximately 800 μm, indicating that the optical response remains well confined within the designed operating range.

The lateral focal-spot distributions are shown on the right side of Fig. 2a, where a representative 3×3 region of the array is presented. Array-level measurements further confirmed highly uniform focal-spot characteristics across the fabricated MeLA, as evidenced by the focal-spot FWHM, normalized intensity, and ellipticity obtained from nine spatially distributed regions of the array (Fig. S5). These results demonstrate that the reduced-pitch MeLA maintains robust lens-to-lens focusing consistency over a large-area aperture. For light-field operation, the system operating plane is defined by the array-level spatial arrangement of the elemental sampling patterns needed to maintain $f^{\#}$ matching, rather than by the position of maximum focal intensity alone. At the peak-intensity plane near 1240 μm, adjacent elemental patterns remain spatially separated, leading to incomplete spatial–angular sampling. At the designed operating plane near 1430 μm, the patterns become approximately tangent, establishing the desired $f^{\#}$-matched sampling geometry without appreciable inter-lenslet overlap. Further propagation beyond this plane leads to increasing overlap between neighboring patterns (Fig. S6). Accordingly, the MetaLFM imaging experiments were performed near 1430 μm, where the system achieves the required $f^{\#}$-matched sampling geometry while retaining sufficient focal intensity for image formation.

The intensity profiles along the x, y, and z directions for a single lens are shown in Fig. 2b, where the simulated (blue) and experimental (red) curves are used to extract the corresponding FWHM

values. The simulated lateral FWHM was 10.0 μm in both x and y, compared with measured values of 10.2 ± 0.2 μm and 10.1 ± 0.2 μm (n = 30), respectively. The axial FWHM was 802.0 μm in simulation and 810.3 ± 12.0 μm experimentally, further validating the designed focal characteristics. We next evaluated how these properties translate into volumetric imaging performance in MetaLFM.

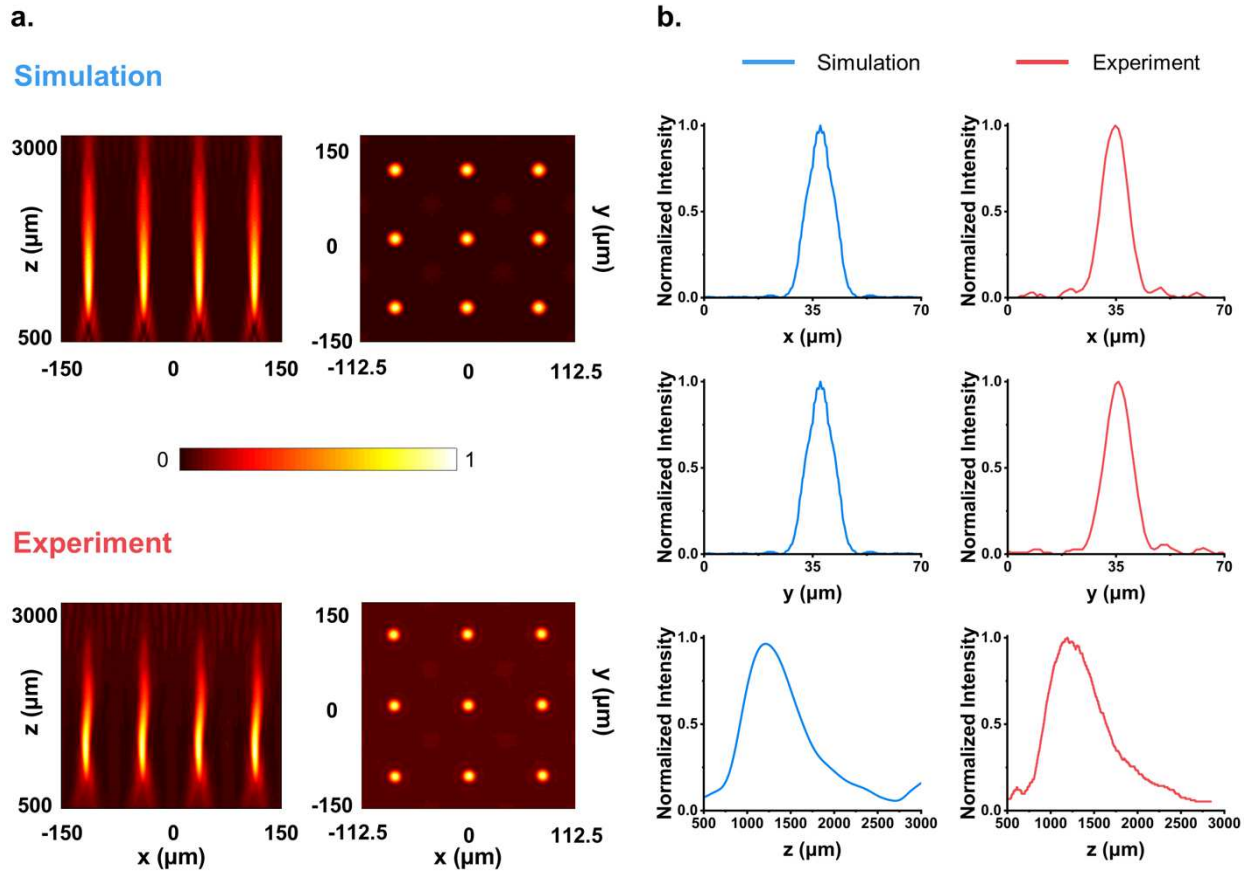


Figure 2. Focusing characterization of the MeLA. (a) Simulated and experimental two-dimensional intensity distributions in the axial (left, x-z) and lateral (right, x-y) directions. The top panels show the simulated results and the bottom panels show the corresponding experimental results. Only representative regions from the lens array are shown. (b) One-dimensional cross-sectional intensity profiles for a single lens. The left panels show the simulated results and the right panels show the corresponding experimental results.

2.2. Resolution characterization of MetaLFM

To quantify the imaging performance of MetaLFM, we first characterized its reconstructed 3D PSF and compared it with conventional LFM under the same optical configuration. Fluorescent beads with a diameter of 0.5 μm were embedded in 1% agarose and imaged using both systems to characterize the reconstructed 3D PSF. The beads were randomly distributed throughout the agarose volume, and the reconstructed imaging volume was approximately 250 × 250 × 80 μm³ (Fig. 3a and Fig. S7). For quantitative PSF analysis, a more dilute bead preparation (1:80000) was used to obtain spatially isolated emitters, and the FWHM of the reconstructed bead profiles was used to estimate lateral and axial resolution.

Representative reconstructed PSFs show narrower lateral and axial profiles with MetaLFM than with conventional LFM (Fig. 3b). Because grid-like reconstruction artifacts are most pronounced near the native image plane [7,8,27] and can interfere with reliable PSF-width estimation, quantitative measurements were performed at axial offsets away from z = 0 (Fig. 3b, left), where individual bead profiles could be reliably resolved. At z = +10 μm toward the objective (Fig. 3b, middle), MetaLFM achieved lateral and axial resolutions of 2.1 ± 0.1 μm and 9.4 ± 0.5 μm, respectively, compared with 2.6 ± 0.4 μm and 10.4 ± 0.5 μm for conventional LFM. At a larger axial offset of z = +30 μm (Fig. 3b, right), the difference became more pronounced: MetaLFM achieved 4.3 ± 0.3 μm laterally and 16.5 ± 0.3 μm axially, whereas conventional LFM yielded 5.7 ± 0.4 μm and 21.7 ± 1.2 μm, respectively (mean ± SD, n = 7 beads).

We next examined whether the PSF improvement was maintained throughout the usable imaging range rather than being restricted to selected axial positions. Measurements across the system DOF showed consistently narrower reconstructed profiles for MetaLFM in both lateral and axial dimensions (Fig. 3c), with the corresponding quantitative values summarized in Supplementary

Table 2. Across the evaluated depth range, MetaLFM reduced the lateral and axial FWHM by up to 44% and 39%, respectively, relative to conventional LFM, with the relative benefit generally becoming more pronounced at larger axial offsets from the native image plane. This PSF-based result was further supported by USAF resolution-target imaging (Fig. S8), where MetaLFM maintained the resolvability of the 3.91-μm line-width pattern of group 7-1 across the evaluated range and preserved its characteristic modulation more consistently than conventional LFM. Together, the bead and USAF measurements demonstrate more consistent spatial resolution with MetaLFM throughout the investigated axial range.

We next compared MetaLFM with previously reported conventional LFM implementations to place its performance within the broader resolution–depth landscape (Fig. 3d). The comparison includes state-of-the-art approaches reported in [6,7,9,12–14,27–35], with detailed system parameters summarized in Supplementary Table 3. Several previous approaches achieve improved spatial resolution through optimized illumination strategies or the use of higher-magnification objective lenses; however, these gains are often accompanied by a reduction in accessible imaging depth. More broadly, LFM performance is constrained by a trade-off between spatial resolution and imaging depth. By increasing sampling density through the MeLA while retaining a practical depth range, MetaLFM shifts this trade-off toward a more favorable operating regime, providing competitive spatial resolution together with comparatively broad volumetric coverage.

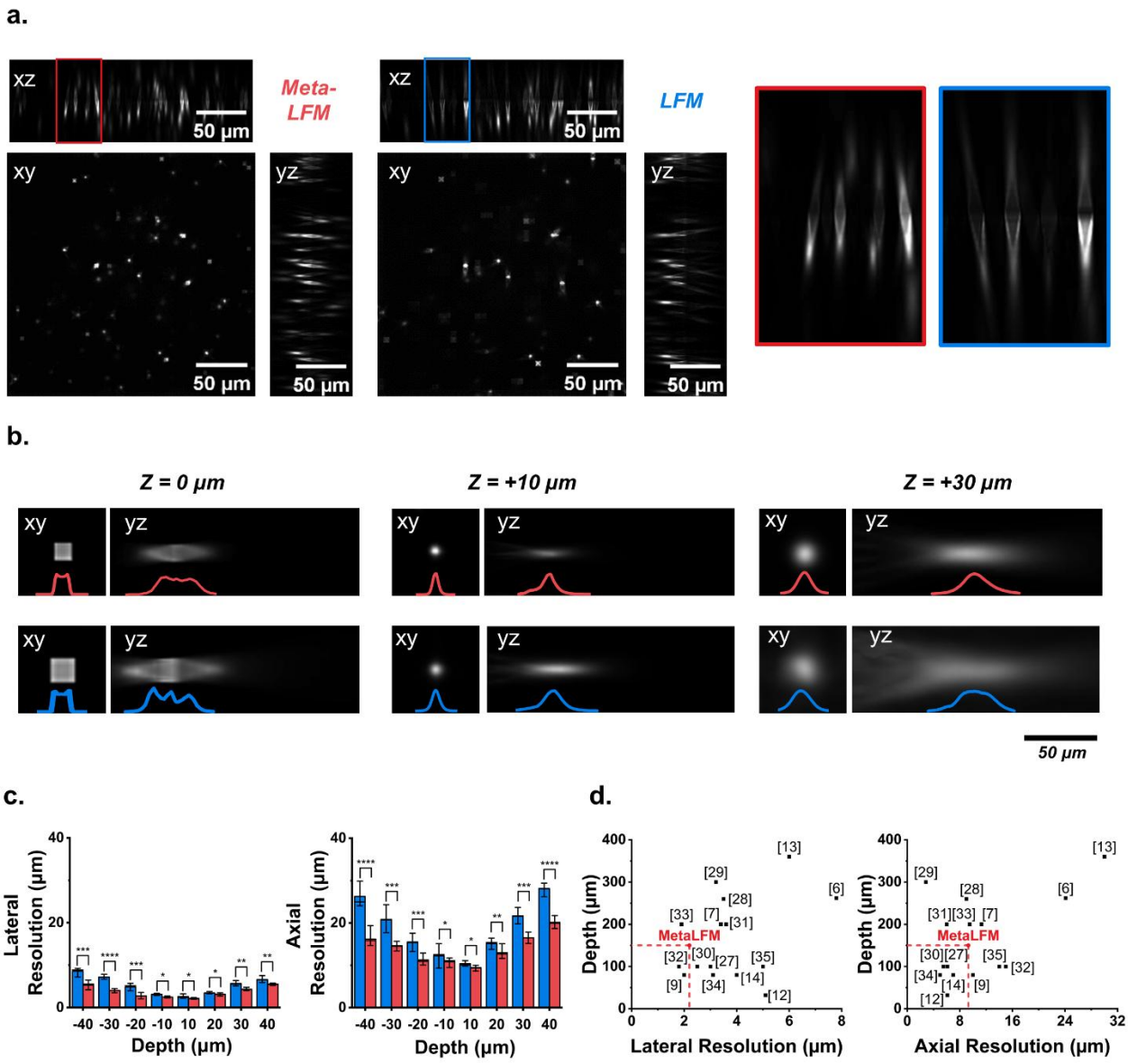


Figure 3. PSF characterization of MetaLFM. (a) Maximum-intensity projection (MIP), XZ and YZ views from experimental PSF validation using 0.5-μm fluorescent beads embedded in agarose, imaged and reconstructed with MetaLFM and conventional LFM. The zoomed-in regions for MetaLFM and LFM, marked by the red and blue rectangles, respectively, show improved axial bead reconstruction with MetaLFM. (b) Corresponding reconstructed PSFs of representative beads at three axial positions toward the objective lens. (c) Lateral and axial resolution comparison between MetaLFM and LFM across the same depth range, showing sustained resolution improvement of MetaLFM over conventional LFM. P values were calculated by two-sided paired t-test, "" indicates $p < 0.05$, "**" indicates $p < 0.01$, "***" indicates $p < 0.001$ and "****" indicates $p < 0.0001$. (d) Comparison with state-of-the-art conventional LFM implementations from the relevant references, highlighting the resolution–depth trade-off and the*

operating regime enabled by MetaLFM. References labeled within the plot correspond to methods achieving improved resolution performance.

2.3. Volumetric neuroimaging of ex vivo mouse spinal cord tissue

Having demonstrated consistent PSF improvements across depth, we next investigated the advantages of MetaLFM in volumetric imaging of intact neural tissue. The spinal cord is a central component of the nervous system responsible for transmitting motor and sensory signals between the brain and peripheral tissues, and its function relies on densely organized neuronal networks distributed across 3D tissue volumes [36]. Resolving the structural organization of these networks requires imaging approaches capable of capturing fine neuronal features, including dendrites and axonal projections, within intact tissue. To investigate the capability of MetaLFM in this context, we applied it to volumetric imaging of ex vivo mouse spinal cord sections (~25 μm thick, Fig. 4a).

Motor neuron structures were resolved throughout the section thickness, enabling 3D reconstruction of neuronal morphology from a single acquisition (Fig. 4a, purple square). To directly assess structural fidelity, dendrites located near the edge of the spinal cord section were analyzed using MetaLFM and conventional LFM within identical ROIs. Compared with LFM, MetaLFM shows reduced elongation artifacts and improved structural definition in orthogonal XZ and YZ views (Fig. 4b and Fig. S9; brown square in Fig. 4a).

To quantify these differences, cross-sectional intensity profiles were measured at six positions within the ROI shown in Fig. 4b. In all cases, MetaLFM exhibited smaller FWHM values than LFM, indicating improved structural resolution (Fig. 4c). We further performed statistical analysis across 15 randomly selected ROIs (6 dendrites measured from each of these ROIs; Fig. 4d), which

revealed a significant reduction in lateral FWHM for MetaLFM, corresponding to an average 25% reduction in the cross-sectional dendrite width relative to LFM.

In addition, we analyzed a second ROI within the spinal cord section characterized by higher neuronal density (Fig. 4e, green square in Fig. 4a). Enlarged ROI (1) and (2) from the reconstructed maximum-intensity projections (MIPs) of both MetaLFM and LFM are shown below. These additional ROIs indicate that the resolution advantage of MetaLFM is preserved in regions with higher neuronal density.

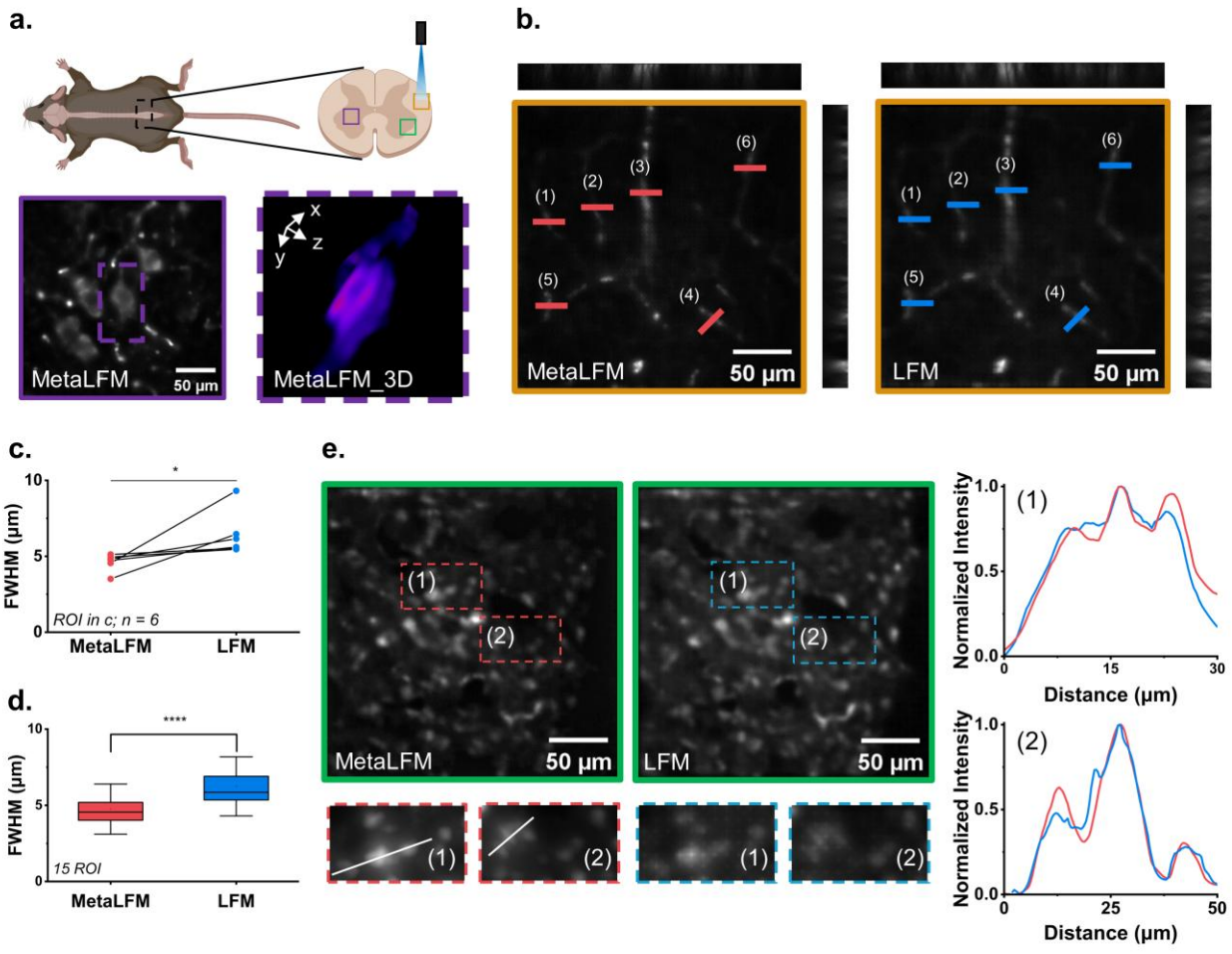


Figure 4. Volumetric neuroimaging of ex vivo mouse spinal cord tissue. (a) MetaLFM-based volumetric reconstruction of a fixed mouse spinal cord section (~25 μm thick) showing motor neuron structures across the tissue thickness from a single acquisition;

the ROI marked by the purple square is shown as a 3D volume rendering. (b) Direct comparison of MetaLFM and conventional LFM in identical ROIs near the tissue edge, marked by the brown square in (a), shown as MIP and XZ/YZ views. (c) Representative dendrite cross-sectional intensity profiles (FWHM) at six positions marked in (b), showing narrower profiles with MetaLFM. (d) Statistical analysis across multiple ROIs (15 ROIs; 6 dendrites per ROI) demonstrating reduced lateral FWHM for MetaLFM relative to conventional LFM. (e) Additional ROI in a denser neuronal region, marked with green in (a), demonstrating structural improvement with MetaLFM in MIP and profile comparisons. P values were calculated by two-sided paired t-test, "" indicates $p < 0.05$ and "****" indicates $p < 0.0001$*

2.4. Volumetric imaging of fixed human intestinal organoids

Following the validation in mouse spinal cord sections, we next applied MetaLFM to imaging of fixed human intestinal organoids, which can reach dimensions of several hundred micrometers and therefore present a challenging target for depth-resolved imaging. Organoids are widely used as 3D in vitro models that recapitulate key aspects of tissue architecture and cellular organization, supporting applications in developmental biology, disease modeling, and drug screening [37,38]. Resolving their internal organization requires imaging methods capable of distinguishing fine spatial features throughout an extended 3D volume. Conventional wide-field microscopy provides direct fluorescence imaging with relatively simple acquisition, but its limited axial discrimination causes out-of-focus signals from different depths to overlap when imaging thick specimens, making depth-resolved visualization challenging. Optical-sectioning approaches such as confocal, multiphoton, and light-sheet microscopy can overcome this limitation and provide high-quality 3D imaging; however, they generally require sequential spatial or axial acquisition and therefore involve trade-offs among imaging speed, spatial resolution, imaging depth, and photodamage [39]. Building on the single-shot volumetric capability of LFM, MetaLFM improves spatial sampling to enable higher-resolution volumetric reconstruction without sequential axial scanning.

We first imaged the whole targeted organoid using wide-field fluorescence microscopy with a 10×/0.3 NA objective (Fig. 5a). A selected region (marked b in Fig. 5a) was subsequently acquired with the light-field system and reconstructed using both MetaLFM and conventional LFM with five iterations (Fig. 5b). The resulting volume covered approximately 250 × 250 × 150 μm³. This axial extent corresponds to the depth of view (DOV), defined as the usable range recovered by deconvolution and therefore extending beyond the theoretical DOF (Supplementary Note 1). Along the corresponding lines used for XZ and YZ cross-sectional extraction (white dashed lines), MetaLFM shows a substantial reduction in the grid-like artifacts that are typically observed in conventional LFM reconstructions, due to the reduced metalens pitch. To further examine structural details, we zoomed into 4 identical ROIs for both techniques and analyzed the intensity profiles of the characteristic honeycomb-like structures within the organoid (Fig. S10).

We further imaged another region of the organoid (marked **c.** in Fig. 5a). A 3D rendering of this region is shown in Fig. 5c. For quantitative fidelity analysis, reconstructed slices were extracted from z = −72 to +72 μm at 18-μm intervals for both MetaLFM and LFM, while corresponding wide-field images were acquired at the same axial positions by sample scanning (Fig. 5d). Image fidelity was assessed using structural similarity index (SSIM) and peak signal-to-noise ratio (PSNR) across 7 randomly imaged ROIs, with wide-field images acquired from the same optical platform serving as a reference for relative structural consistency, rather than absolute ground truth. MetaLFM consistently achieved higher SSIM and PSNR values across the depth range, indicating improved reconstruction fidelity compared with conventional LFM.

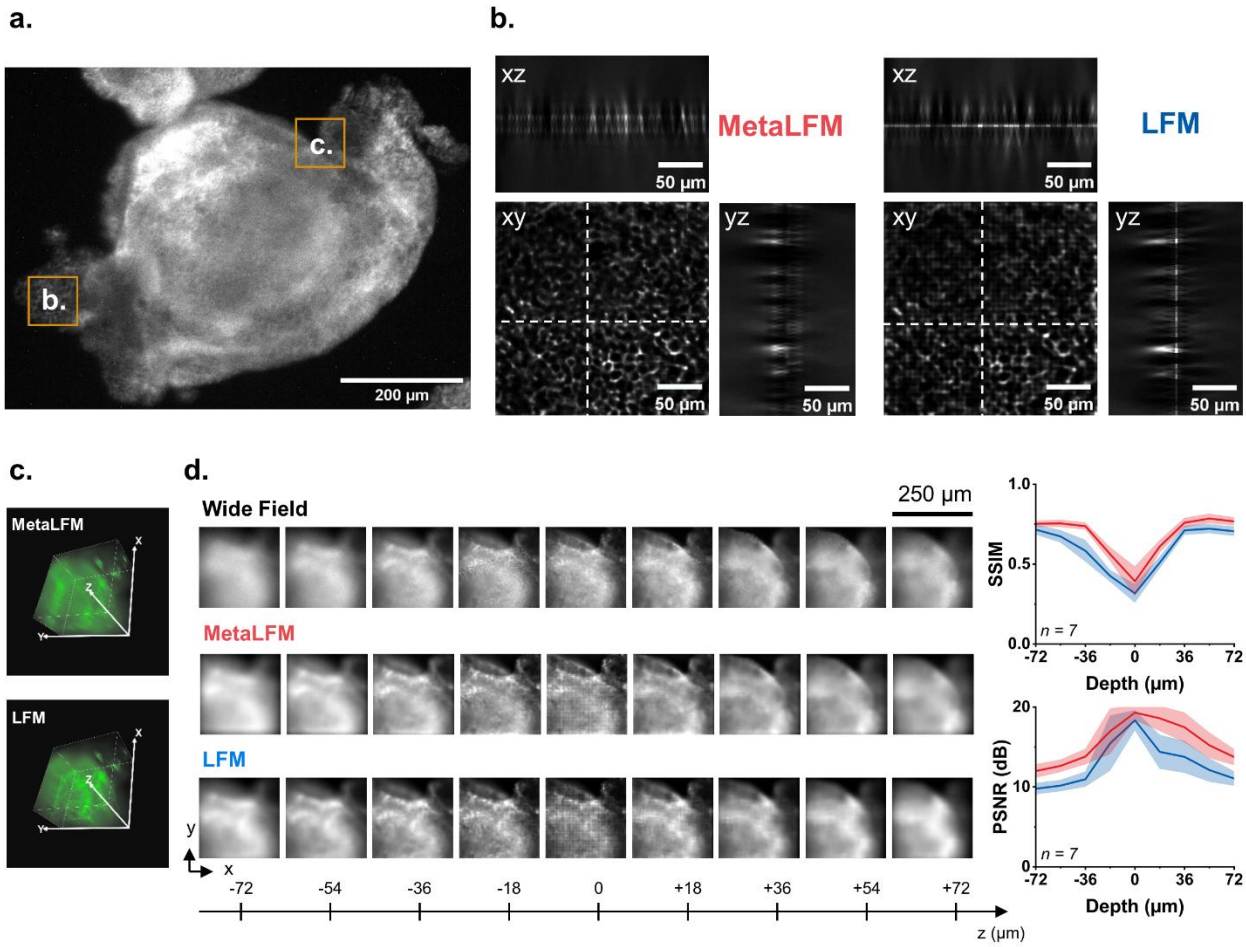


Figure 5. Volumetric imaging of fixed intestinal organoids. (a) Wide-field image of the targeted intestinal organoid acquired with a 10×/0.3 NA objective to identify ROIs for volumetric reconstruction. (b) MetaLFM and conventional LFM reconstructions of the same ROI (marked in panel a) at a representative axial plane z = +10 μm. Corresponding XZ/YZ cross-sections show reduced grid-like artifacts in MetaLFM. (c) 3D volume rendering of a second ROI (marked in panel a), demonstrating volumetric structural organization. (d) Quantitative fidelity evaluation across depth: reconstructed slices extracted over the indicated depth range and compared to corresponding wide-field images using SSIM and PSNR, based on measurements across 7 ROIs, showing consistently higher reconstruction fidelity for MetaLFM. Shaded regions represent standard deviation.

2.5. High-speed calcium imaging

To evaluate the capability of MetaLFM for functional imaging, we performed calcium imaging of cultured primary cortical neurons labeled with the fluorescent calcium indicator Fluo-4. Structural

imaging of neurons expressing the neuronal marker TUBB3 revealed clearly resolved neuronal morphology, including soma, dendrites, axons, and axon terminals within the reconstructed volume (Fig. 6a). We next examined the depth-resolved distribution of calcium-active neurons at 25 Hz over $z = -25$ to $+25$ μm relative to the nominal focal plane. Individual neurons were identified and spatially annotated in the corresponding reconstructed planes (Fig. 6b). Neurons remained detectable throughout this range, indicating preservation of functional signal across the accessible imaging volume.

Among the reconstructed planes, the $z = 0$ μm plane contained the largest number of simultaneously observable neurons and was therefore selected for quantitative analysis. Using automated segmentation and signal extraction, fluorescence time series were obtained from ten neurons identified within this plane (Fig. 6c). Calcium signals were quantified as relative fluorescence changes ($\Delta F/F$). The extracted traces revealed spontaneous transients across multiple neurons, including both isolated events and coordinated bursts.

To visualize population-level dynamics, we generated a kymograph of calcium signals across the detected neurons (Fig. 6c, right). The kymograph revealed intermittent synchronized events involving simultaneous signal elevations across multiple cells, interspersed with periods of lower activity. Together with the individual traces, these data demonstrate that MetaLFM can resolve both single-cell calcium transients and coordinated network activity.

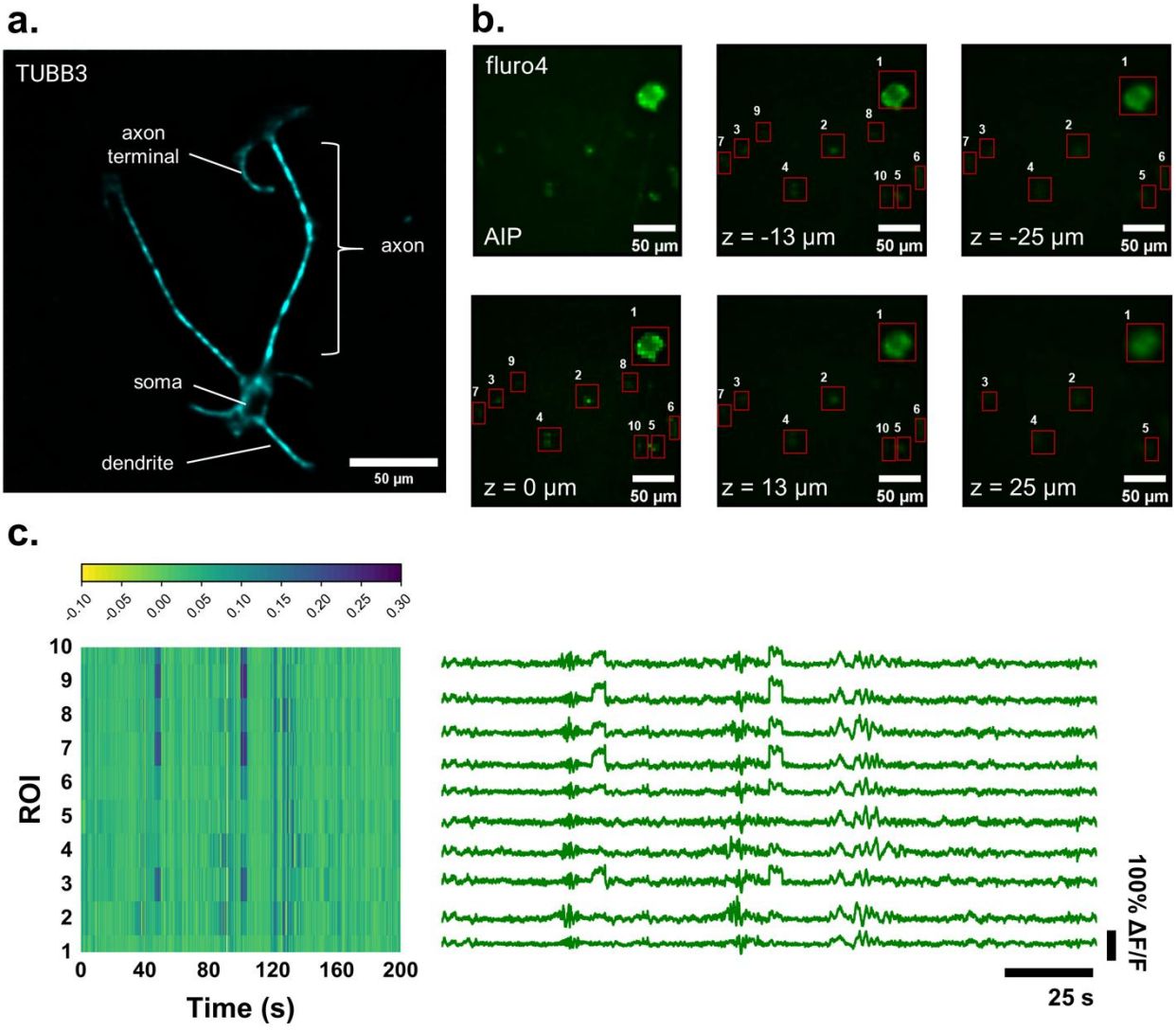


Figure 6. High-speed volumetric calcium imaging. (a) Structural imaging of cultured primary cortical neurons labeled with Fluo-4 and immunostained for the neuronal marker TUBB3, showing clearly resolved fine neuronal morphology at z = +10 µm. (b) Average intensity projection (AIP) and depth-resolved identification of calcium-active neurons across a reconstructed range of 50 µm, with neuron positions annotated in each plane. (c) Kymograph summarizing population activity across detected neurons over time, revealing intermittent synchronized events and heterogeneous dynamics within the cultured network and representative ΔF/F calcium traces extracted from neurons in the selected plane (z = 0 µm), showing spontaneous activity patterns.

3. Discussion

The observed performance gains originate from the metalens-enabled optical sampling architecture, which provides wavefront control beyond the geometric constraints of conventional refractive microlens arrays. The planar metasurface architecture decouples lens pitch from focal length, allowing reduced sampling pitch without requiring proportionally shorter focal lengths. This avoids curvature and sag-height limitations inherent to refractive microlenses and enables high-density angular sampling while preserving numerical aperture and depth coverage. This design shifts the conventional resolution–depth trade-off of LFM toward a more favorable regime that is difficult to realize using refractive MLA implementations.

Reduction of grid-like reconstruction artifacts near the native focal plane is a consistent feature of the proposed approach. This effect is evident in intestinal organoid imaging (Fig. S11), where MetaLFM exhibits smoother structural representation than conventional LFM. Quantitative analysis of the characteristic spatial periodicity indicates an approximately 1.4-fold reduction for MetaLFM. This behavior is consistent with the denser sampling provided by the reduced-pitch MeLA, which helps mitigate reconstruction aliasing near the native focal plane and improves structural fidelity.

Despite these improvements, several limitations remain. The current system depends on computational reconstruction quality, including accurate calibration and forward-model matching. Large-area fabrication uniformity may affect lens-to-lens consistency, and the demonstrated implementation was validated under specific optical and spectral conditions rather than across a broader range of wavelengths or imaging configurations. Addressing these factors will be important for broader adoption and further performance scaling.

Future work should prioritize scalable fabrication strategies that improve array-level uniformity across larger apertures [17]. Extensions toward wavelength-multiplexed [40] or polarization-multiplexed [41] operation could further expand the functionality of metasurface-based light field imaging. In parallel, integrating advanced computational reconstruction frameworks, including learning-based approaches, may accelerate volumetric reconstruction while preserving image fidelity [42,43]**.** Improvements in detector technology, such as higher frame-rate cameras or adaptive region-of-interest acquisition, could further enhance temporal resolution for dynamic imaging [44,45]. Overall, these results support metalens-array-based light field microscopy as a promising route toward compact, high-speed, and high-fidelity volumetric bioimaging systems.

4. Materials and methods

4.1. Design and Fabrication of a MeLA

The MetaLFM system was implemented by modifying a home-built platform (Fig. 1a). Optical setup parameters, including the objective lens, tube lens, camera, laser and MLA are summarized in Supplementary Table 4, and the optical design and parameter calculations of the MeLA are described in Supplementary Note 1.

The MeLA was designed based on the following key specifications. The target wavelength of the microscopy system is 525 nm. Based on parameter calculations tailored for light field microscopy, the MeLA has an $f^{\#}$ of 20 and a numerical aperture (NA) of 0.025. Each lens has a circular aperture with a focal length of 1430 μm and an aperture diameter of 71.5 μm, and identical lenses are periodically repeated to form a 60×60 array. The gap between adjacent lenses is set to 3.5 μm, resulting in a lens pitch of 75 μm. The detailed design is described in Supplementary Note 2 and Fig. S1.

TiO_2 was selected as the nanopost material due to its high refractive index contrast compared to a quartz substrate, with a refractive index of approximately n = 2.456 at 525 nm. The upper panel of Fig. 1c shows the transmission and phase responses as functions of the diameter of the nanopost for a single unit cell that makes up the MeLA. The inset presents a side view of the unit cell, where D, h, and p denote the diameter and height of the nanopost and the period of the unit cell, respectively.

The unit cell of the metalens was numerically simulated using Ansys Lumerical FDTD. In the simulation, periodic boundary conditions were applied along the x- and y-directions, while perfectly matched layers (PMLs) were applied along the z-direction. A plane wave at 525 nm was incident from the quartz substrate side onto the nanoposts. The period was chosen to satisfy both the Nyquist theorem and the subwavelength condition, while the height was determined based on fabrication feasibility and the corresponding aspect ratio. Therefore, the height of the nanopost and the period of the unit cell were fixed at h = 600 nm and p = 250 nm, respectively, while the diameter D was swept from 100 nm to 220 nm to extract the transmission amplitude and the corresponding phase. As a result, transmission and phase maps as functions of D were obtained. To ensure high transmission for all selected unit cells, a threshold condition of transmission > 0.8 was applied. Here, transmission was defined as $|t_x|/n_{SiO2}$, where t_x is the transmission coefficient for the x-polarized component. As shown in Fig. 1c, diameters in the range of 100–206 nm satisfy this criterion (blue line), and the corresponding phase, after phase wrapping, spans nearly a full 2π range (red line).

Based on the phase map derived from the unit cell properties (Fig. 1c, bottom), the nanoposts are arranged to satisfy the required hyperbolic phase profile given by

$$\phi(x,y) = 2\pi - \frac{2\pi}{\lambda}\left(\sqrt{x^2+y^2+f^2} - f\right) \qquad (1)$$

where f is the focal length of a single lens and λ is the target wavelength of 525 nm. In addition, the diameters of the nanopost are selected such that the complex transmission coefficient t_x at each position matches the required hyperbolic phase profile [46,47]. Further detailed information for the design of the MeLA is provided in the Supplementary Note 2.

Finally, the single metalens is replicated in a 60 × 60 array to form a full MeLA with a total size of 4.5 mm × 4.5 mm. To fabricate the MeLA, a 600-nm-thick TiO_2 film is deposited on a 500-μm-thick quartz substrate. The thickness of TiO_2 is controlled within ±5% and measured by an ellipsometer. A positive resist is coated onto the TiO_2 layer, and the MeLA pattern is generated by electron-beam lithography. After development, a 50-nm-thick Cr layer is deposited over the entire surface, followed by a lift-off process to form a Cr hard mask. The TiO_2 layer is subsequently dry-etched using the Cr mask. The final structures are confirmed by SEM (Fig. 1d).

To quantitatively evaluate the focusing performance of the MeLA, numerical simulations were performed using the convolution-based Rayleigh–Sommerfeld diffraction equation [48].

The propagated field at an axial distance z was calculated as

$$\psi(x,y,z) = \mathcal{F}^{-1}\left\{\mathcal{F}[\psi(u,v,0)]\,\mathcal{F}\left[\frac{ik}{2\pi}\frac{e^{ikr'}}{r'}\frac{z}{r'}\left(1-\frac{1}{ikr'}\right)\right]\right\}, \quad r' = \sqrt{u^2+v^2+z^2} \qquad (2)$$

where $\mathcal{F}$ and $\mathcal{F}^{-1}$ denote the Fourier and inverse Fourier transforms, respectively.

4.2. Animals and human-derived materials

The handling of animals was conducted in accordance with the guidelines of the Institutional Animal Care and Use Committee board (IACUC) of the Gwangju Institute of Science and Technology (GIST), South Korea. Experimental protocols were approved by the Laboratory Animal Resource Center (LARC) at GIST under protocol #GIST-2025-031. This study utilized 4 adult C57BL/6 mice (8–10 weeks old, 24–28 g), which were housed with food and water ad libitum under a standard 12-hour light/dark cycle. All mice were bred at the GIST animal facility. Before brain harvesting, carbon dioxide (CO_2) euthanasia was performed in a dedicated chamber by the gradual displacement of air, followed by cervical dislocation to ensure death. This procedure was conducted to minimize suffering, adhering to the AVMA Guidelines for the Euthanasia of Animals (2020). The study is reported in accordance with the ARRIVE guidelines (https://arriveguidelines.org), ensuring transparency and rigor in the design, conduct, and reporting of the animal experiments. Human induced pluripotent stem cell (iPSC)-derived colon organoids used in this study were obtained from commercial suppliers. All cell lines were generated by the provider under appropriate ethical approvals, including informed donor consent, and in compliance with relevant institutional and national regulations. No new human samples were collected for this study, and all experiments were conducted in accordance with the supplier's material transfer and ethical use guidelines.

4.2.1. Cultured primary cortical neurons

Cortical tissue was collected from adult mice (8–10 weeks old) and dissociated with 100 U papain (P4762, Sigma-Aldrich) followed by collagenase II (1 mg/ml; 11179179001, Roche) and dispase II (1.2 mg/ml; 04942078001, Roche) for 20 minutes at 37 °C. The tissues were then triturated in Hanks' balanced salt solution containing 10 mM glucose and 5 mM HEPES (pH 7.35) using a fire-

polished Pasteur pipette to obtain a single-cell suspension. Dissociated cortical neuronal cells were filtered through a 40-μm strainer, collected by centrifugation at 1000 g for 8 min, and resuspended in DMEM medium supplemented with B27 (Thermo Fisher Scientific) and Glutamax (Thermo Fisher Scientific). Cells were then seeded on poly-L-ornithine (P4832, Sigma-Aldrich) coated six-well plates in DMEM supplemented with 10% fetal bovine serum, penicillin (20 U/ml), and streptomycin (0.2 mg/ml), and maintained at 37 °C in a humidified incubator with 5% CO_2.

4.2.2. Calcium Imaging Preparation

Primary cortical neurons at 15 days in vitro (DIV 15) were loaded with 2 μM Fluo-4 AM (Invitrogen, Thermo Fisher Scientific) and 0.2% (w/v) F-127 (stock in DMSO) (Sigma) in the modified Ringer's solution (MRS: 150 mM NaCl, 5 mM KCl, 2.5 mM $CaCl_2$, 1 mM $MgCl_2$, 10 mM HEPES, 10 mM D-Glucose, pH adjusted to 7.4 with NaOH) for 30-45 minutes at 37ºC, followed by three washes and a 10 min deesterification period in the modified Ringer's solution. Cells were imaged using the MetaLFM setup described above. Neurons were illuminated at 475 nm, and time-lapse images were acquired for 2 min per ROI. Fluorescence intensity was quantified using ImageJ. Intracellular calcium dynamics were expressed as $\Delta F/F_0$, where F_0 denotes baseline fluorescence.

4.2.3. Immunocytochemistry

Cultured cells were washed in PBS, fixed in 4% paraformaldehyde (PFA) for 20 min, and permeabilized with 0.1% Triton X-100. After blocking in 5% normal goat serum, bovine serum albumin (1 mg/ml; BSA), and 0.3% Triton X-100 in PBS for 1 hour at room temperature, cells were incubated with primary antibodies in 5% donkey serum and BSA (1 mg/ml) in PBS overnight at 4°C. Secondary antibodies (raised in goat, 1:1000, Jackson ImmunoResearch) were applied for

1 hour at room temperature. Coverslips were mounted with Fluoromount Aqueous Mounting Medium (F4680, Sigma-Aldrich).

4.2.4. Immunofluorescence

Anesthetized mice were fixed via transcardial perfusion with PBS followed by 4% (w/v) paraformaldehyde (PFA, RNase-free; Bioss, C2055). Spinal cord tissues were freshly dissected and post-fixed in 4% PFA at 4°C overnight. Tissues were cryoprotected in 30% (w/v) sucrose (Sigma-Aldrich, S8501) in PBS for 48 hours, embedded in Tissue-Tek O.C.T. compound (Sakura, 4583), and sectioned at 25 μm using a Leica cryostat (Leica CM1850). Cryo-sections were blocked in 5% goat serum and 0.2% Triton X-100 in PBS for 1 hour at room temperature. Sections were incubated in primary antibodies (diluted in 5% normal goat serum and 0.3% Triton X-100 in PBS) overnight at 4°C, followed by incubation with secondary antibodies for 1 hour at room temperature. Primary antibodies included mouse anti-NeuN (1:500, Abcam), and DAPI for counterstaining (Thermo Fisher Scientific). Slides were mounted with Prolong Gold antifade reagent (Invitrogen, P36931) and imaged based on the need.

4.2.5. Intestinal organoid culture and differentiation

Human intestinal organoids were generated from commercially available human iPSC-derived colon organoids (SCC300, Merck Millipore). Cryopreserved organoids were thawed and embedded in growth factor–reduced Matrigel (356231, Corning) and seeded as 20-μL domes (three domes per well) in 24-well plates. After polymerization at 37 °C for 20 min, 1.5 mL of organoid culture medium was added to each well. Human colon organoid culture medium consisted of Advanced DMEM/F12 (12634-010, Gibco) supplemented with penicillin–streptomycin, 2 mM GlutaMAX (35050-061, Gibco, Thermo Fisher Scientific), 1× B27

supplement (minus vitamin A, 12587-010, Gibco), 1× N2 supplement (17502-048, Gibco), 50% L-WRN conditioned medium, gastrin I (G9020, Sigma-Aldrich), A-83-01 (SML0788, Sigma-Aldrich), recombinant human epidermal growth factor (236-EG, R&D Systems), and Primocin (ant-pm-05, InvivoGen), as previously described [49,50]. L-WRN conditioned medium was prepared from an L-WRN fibroblast cell line (CRL-3276, ATCC) following published protocols [49,50]. Y-27632 (10 μM) was added only during initial seeding. Culture medium was replaced every other day. Organoids were passaged every 5–7 days by mechanical disruption of Matrigel followed by dissociation using TrypLE Express (12604-013, Gibco, Thermo Fisher Scientific). Cells were resuspended in fresh Matrigel and replated as 20-μL domes at a split ratio of 1:10. For differentiation, organoids were expanded for 4 days in L-WRN-containing medium and subsequently cultured for ~10 days in differentiation medium lacking L-WRN conditioned medium, with medium changed every other day.

4.2.6. Fluorescent staining of intestinal organoids

For immunofluorescence staining, differentiated organoids were harvested by mechanical disruption of Matrigel in cold PBS and fixed in 4% paraformaldehyde for 30 min at room temperature. Fixed organoids were washed twice with PBS and permeabilized with 0.1% Triton X-100 (T8787, Sigma-Aldrich) for 30 min. Samples were then blocked in PBS containing 0.1% Triton X-100 and 1% normal goat serum (50197Z, Thermo Fisher Scientific) for 1 h at room temperature. Organoids were incubated overnight at 4 °C with primary antibody against β-catenin (ab32572, Abcam) diluted in blocking buffer. The following day, samples were washed twice with blocking buffer and incubated for 1 h at room temperature with Alexa Fluor 488–conjugated

secondary antibody (A11034, Invitrogen). After three washes with PBS, stained organoids were stored in PBS at 4 °C until 3D imaging.

4.3. Light field reconstruction and analysis

Light-field reconstruction was performed using a wave-optics-based deconvolution framework described in [7,8], implemented using the software package provided in [7]. All data processing and analysis were accomplished with MATLAB (MathWorks, MATLAB 2019a), ImageJ (Version 1.54p) and Origin (OriginLab, Origin 2022).

Code Availability

The code used for calcium-imaging analysis in Fig. 6 is publicly available at https://github.com/zamanashiq3/High-Speed-Volumetric-Ca-Imaging-Analysis-Pipeline

Data Availability

All data needed to evaluate the conclusions of this study are available in the paper and/or the Supplementary Materials, and additional data are available from the corresponding author upon reasonable request.

Acknowledgements

This work was supported by the National Research Foundation of Korea (NRF) funded by the Korean government (MSIT) (Nos. RS-2023-00264409, RS-2023-00302281, and RS-2025-00522868), the Ministry of Trade, Industry and Energy (MOTIE), Korea, under the Global Industrial Technology Cooperation Center (GITCC) program supervised by the Korea Institute for Advancement of Technology (KIAT) (Task No. P0028474), the Institute of Information & Communications Technology Planning & Evaluation (IITP) grant funded by the Korean

government (MSIT) (No. 2019-0-01842), supported by the NRF grant (RS-2022-NR072263) and the InnoCORE program of the Ministry of Science and ICT (GIST InnoCORE KH0860). We would like to thank Nguyen Tat Thanh University, Ho Chi Minh City, Vietnam for the support of time and facilities for this study.

Conflict of Interest

The authors declare no conflicts of interest.

Author Contributions

Tien Nhat Nguyen: Writing – original draft, Methodology, Investigation. **Doyoon Lee:** Writing – original draft, Methodology, Investigation. **Huu Lam Phan:** Formal analysis. **Akm Ashiquzzaman:** Software, Resources. **Yesl Jun:** Resources. **Minkyung Kim:** Writing – review and editing, Conceptualization. **Euiheon Chung:** Writing – review and editing, Conceptualization

References

1. Xiao, S. *et al.* Large-scale deep tissue voltage imaging with targeted-illumination confocal microscopy. *Nat. Methods* **21**, 1094–1102 (2024).

2. Xiao, S., Giblin, J. T., Boas, D. A. & Mertz, J. High-throughput deep tissue two-photon microscopy at kilohertz frame rates. *Optica* **10**, 763–769 (2023).

3. Gong, C. *et al.* Hybrid solid−liquid optics enable scalable, high-resolution light-sheet microscopy across diverse immersion media. *Nat. Biotechnol.* https://doi.org/10.1038/s41587-026-03172-7 (2026) doi:10.1038/s41587-026-03172-7.

4. Mac, K. D. *et al.* Rapid axially scanned and de-scanned line-scan confocal microscopy with a tunable acoustic gradient index of refraction lens for high-speed volumetric *in vivo* imaging. *Neurophotonics* **12**, 045013 (2025).

5. Nguyen, T. N. *et al.* Ultrafast optical imaging techniques for exploring rapid neuronal dynamics. *Neurophotonics* **12**, S14608 (2025).

6. Levoy, M., Ng, R., Adams, A., Footer, M. & Horowitz, M. Light Field Microscopy. *ACM Trans. Graph* **25**, 924–934 (2006).

7. Prevedel, R. *et al.* Simultaneous whole-animal 3D imaging of neuronal activity using light-field microscopy. *Nat. Methods* **11**, 727–730 (2014).

8. Broxton, M. *et al.* Wave optics theory and 3-D deconvolution for the light field microscope. *Opt. Express* **21**, 25418–25439 (2013).

9. Geng, Q., Fu, Z. & Chen, S.-C. High-resolution 3D light-field imaging. *J. Biomed. Opt.* **25**, 106502 (2020).

10. Kim, C. & Lee, M. Design, fabrication, and optical imaging performance comparison of precision microlens arrays for application in plenoptic microscopy systems. *Sci. Rep.* **15**, 36567 (2025).

11. Choi, I. S. *et al.* Strain-tunable optical microlens arrays with deformable wrinkles for spatially coordinated image projection on a security substrate. *Microsyst. Nanoeng.* **8**, 98 (2022).

12. Wang, D. *et al.* Hybrid light-sheet and light-field microscope for high resolution and large volume neuroimaging. *Biomed. Opt. Express* **10**, 6595–6610 (2019).

13. Skocek, O. *et al.* High-speed volumetric imaging of neuronal activity in freely moving rodents. *Nat. Methods* **15**, 429–432 (2018).

14. Wang, D., Roy, S., Rudzite, A. M., Field, G. D. & Gong, Y. High-resolution light-field microscopy with patterned illumination. *Biomed. Opt. Express* **12**, 3887–3901 (2021).

15. Lu, Z. *et al.* Long-term intravital subcellular imaging with confocal scanning light-field microscopy. *Nat. Biotechnol.* **43**, 569–580 (2025).

16. Wu, J. *et al.* Iterative tomography with digital adaptive optics permits hour-long intravital observation of 3D subcellular dynamics at millisecond scale. *Cell* **184**, 3318-3332.e17 (2021).

17. Hu, Z. *et al.* Review for optical metalens based on metasurfaces: fabrication and applications. *Microsyst. Nanoeng.* **11**, 189 (2025).

18. Pi, H. *et al.* Levitation and controlled MHz rotation of a nanofabricated rod by a high-NA metalens. *Microsyst. Nanoeng.* **11**, 67 (2025).

19. Park, M.-K. *et al.* Virtual-Moving Metalens Array Enabling Light-Field Imaging with Enhanced Resolution. *Adv. Opt. Mater.* **8**, 2000820 (2020).

20. Fan, Q. *et al.* Trilobite-inspired neural nanophotonic light-field camera with extreme depth-of-field. *Nat. Commun.* **13**, 2130 (2022).

21. Fan, Z. Bin *et al.* A broadband achromatic metalens array for integral imaging in the visible. *Light Sci. Appl.* **8**, (2019).

22. Lin, R. J. *et al.* Achromatic metalens array for full-colour light-field imaging. *Nat. Nanotechnol.* **14**, 227–231 (2019).

23. Chen, M. K. *et al.* A Meta-Device for Intelligent Depth Perception. *Advanced Materials* **35**, 2107465 (2023).

24. Long, Z., Zeng, Y. & Jin, X. End-to-end design of the metalens array imaging system with extended depth of field. *Opt. Express* **33**, 26869–26886 (2025).

25. Zhang, L. *et al.* Multi-target positioning and motion tracking enabled by a compound meta-eye system. *Microsyst. Nanoeng.* **12**, 203 (2026).

26. Zhao, M. *et al.* Phase characterisation of metalenses. *Light Sci. Appl.* **10**, 52 (2021).

27. Truong, T. V *et al.* High-contrast, synchronous volumetric imaging with selective volume illumination microscopy. *Commun. Biol.* **3**, 74 (2020).

28. Nöbauer, T. *et al.* Video rate volumetric Ca2+ imaging across cortex using seeded iterative demixing (SID) microscopy. *Nat. Methods* **14**, 811–818 (2017).

29. Wagner, N. *et al.* Instantaneous isotropic volumetric imaging of fast biological processes. *Nat. Methods* **16**, 497–500 (2019).

30. Madaan, S. *et al.* Single-objective selective-volume illumination microscopy enables high-contrast light-field imaging. *Opt. Lett.* **46**, 2860–2863 (2021).

31. Aimon, S. *et al.* Fast near-whole–brain imaging in adult Drosophila during responses to stimuli and behavior. *PLoS Biol.* **17**, e2006732 (2019).

32. Pégard, N. C. *et al.* Compressive light-field microscopy for 3D neural activity recording. *Optica* **3**, 517–524 (2016).

33. Cohen, N. *et al.* Enhancing the performance of the light field microscope using wavefront coding. *Opt. Express* **22**, 24817–24839 (2014).

34. Fu, Z. *et al.* Light field microscopy based on structured light illumination. *Opt. Lett.* **46**, 3424–3427 (2021).

35. Pan, Z., Lu, M. & Xia, S. Diffraction-Assisted Light Field Microscopy for Microtomography and Digital Volume Correlation with Improved Spatial Resolution. *Exp. Mech.* **59**, 713–724 (2019).

36. Bai, B. *et al.* Spinal Cord-Like Scaffold with Rapid Tissue Integration Enhanced Spinal Cord Nerve Repair. *Advanced Materials* **37**, e05402 (2025).

37. Xu, X. *et al.* Advances and applications of gut organoids: modeling intestinal diseases and therapeutic development. *Life Medicine* **4**, lnaf012 (2025).

38. Velasco, V., Shariati, S. A. & Esfandyarpour, R. Microtechnology-based methods for organoid models. *Microsyst. Nanoeng.* **6**, 76 (2020).

39. Liu, W., Kim, G.-A. R., Takayama, S. & Jia, S. Fourier light-field imaging of human organoids with a hybrid point-spread function. *Biosens. Bioelectron.* **208**, 114201 (2022).

40. Park, C., Jeon, Y., Lee, S., Kim, Y. & Rho, J. Recomposable Layered Metasurfaces for Wavelength-Multiplexed Optical Encryption via Modular Diffractive Deep Neural Networks. *Adv. Funct. Mater.* **n/a**, e23309 (2025).

41. Dai, T. *et al.* Snapshot Mueller spectropolarimeter imager. *Microsyst. Nanoeng.* **9**, 125 (2023).

42. Song, P., Jadan, H. V, Howe, C. L., Foust, A. J. & Dragotti, P. L. Model-Based Explainable Deep Learning for Light-Field Microscopy Imaging. *IEEE Transactions on Image Processing* **33**, 3059–3074 (2024).

43. Zhou, Y., Jin, Z., Zhao, Q., Xiong, B. & Cao, X. Aberration Modeling in Deep Learning for Volumetric Reconstruction of Light-Field Microscopy. *Laser Photon. Rev.* **17**, 2300154 (2023).

44. Guo, R. *et al.* EventLFM: event camera integrated Fourier light field microscopy for ultrafast 3D imaging. *Light Sci. Appl.* **13**, 144 (2024).

45. Yoon, J. *et al.* Event-based optical imaging and reconstruction of in vivo neuronal and vascular dynamics. *PhotoniX* **7**, 21 (2026).

46. Khorasaninejad, M. *et al.* Polarization-Insensitive Metalenses at Visible Wavelengths. *Nano Lett.* **16**, 7229–7234 (2016).

47. Arbabi, A., Horie, Y., Bagheri, M. & Faraon, A. Dielectric metasurfaces for complete control of phase and polarization with subwavelength spatial resolution and high transmission. *Nat. Nanotechnol.* **10**, 937–943 (2015).

48. So, S., Mun, J., Park, J. & Rho, J. Revisiting the Design Strategies for Metasurfaces: Fundamental Physics, Optimization, and Beyond. *Advanced Materials* **35**, 2206399 (2023).

49. Miyoshi, H. & Stappenbeck, T. S. In vitro expansion and genetic modification of gastrointestinal stem cells in spheroid culture. *Nat. Protoc.* **8**, 2471–2482 (2013).

50. VanDussen, K. L. *et al.* Development of an enhanced human gastrointestinal epithelial culture system to facilitate patient-based assays. *Gut* **64**, 911 (2015).

Supplementary Files

This is a list of supplementary files associated with this preprint. Click to download.

- SUPPLEMENTARYMATERIAL.docx